

**This is a self-archived version of an original article. This version may differ from the original in pagination and typographic details.**

**Author(s):** Verlinde, M.; Dockx, K.; Geldhof, S.; König, K.; Studer, D.; Cocolios, T. E.; de Groote, R. P.; Ferrer, R.; Kudryavtsev, Yu.; Kieck, T.; Moore, I.; Nörtershäuser, W.; Raeder, S.; Van den Bergh, P.; Van Duppen, P.; Wendt, K.

**Title:** On the performance of wavelength meters : Part 1 : consequences for medium-to-high-resolution laser spectroscopy

**Year:** 2020

**Version:** Accepted version (Final draft)

**Copyright:** © Springer-Verlag GmbH Germany, part of Springer Nature 2020

**Rights:** In Copyright

**Rights url:** <http://rightsstatements.org/page/InC/1.0/?language=en>

**Please cite the original version:**

Verlinde, M., Dockx, K., Geldhof, S., König, K., Studer, D., Cocolios, T. E., de Groote, R. P., Ferrer, R., Kudryavtsev, Yu., Kieck, T., Moore, I., Nörtershäuser, W., Raeder, S., Van den Bergh, P., Van Duppen, P., & Wendt, K. (2020). On the performance of wavelength meters : Part 1 : consequences for medium-to-high-resolution laser spectroscopy. *Applied Physics B : Lasers and Optics*, 126(5), Article 85. <https://doi.org/10.1007/s00340-020-07425-4>

# On the performance of wavelength meters — Part 1: Consequences for medium- to high-resolution laser spectroscopy

M. Verlinde,<sup>1,\*</sup> K. Dockx,<sup>1</sup> S. Geldhof,<sup>2</sup> K. König,<sup>3</sup> D. Studer,<sup>4</sup> T.E. Cocolios,<sup>1</sup>  
R. de Groote,<sup>2</sup> R. Ferrer,<sup>1</sup> Yu. Kudryavtsev,<sup>1</sup> T. Kieck,<sup>4</sup> I. Moore,<sup>2</sup> W.  
Nörtershäuser,<sup>3</sup> S. Raeder,<sup>5,6</sup> P. Van den Bergh,<sup>1</sup> P. Van Duppen,<sup>1</sup> and K. Wendt<sup>4</sup>

<sup>1</sup>*KU Leuven, Instituut voor Kern- en Stralingsfysica, Celestijnenlaan 200D, 3001 Leuven, Belgium*

<sup>2</sup>*University of Jyväskylä, Department of Physics, FI-40014 Jyväskylä, Finland*

<sup>3</sup>*Technische Universität Darmstadt, Institut für Kernphysik, 64289 Darmstadt, Germany*

<sup>4</sup>*Johannes Gutenberg-Universität, Institut für Physik, D-55099 Mainz, Germany*

<sup>5</sup>*Helmholtz-Institut Mainz, D-55128 Mainz, Germany*

<sup>6</sup>*GSI Helmholtzzentrum für Schwerionenforschung GmbH, D-64291 Darmstadt, Germany*

Present-day laser-spectroscopy experiments increasingly rely on modern commercial devices to monitor, stabilize and scan the wavelength of their probe laser. Recently, new techniques are capable of achieving unprecedented levels of precision on atomic and nuclear observables, pushing these devices to their performance limits. Considering the fact that these observables themselves are deduced from the frequency difference between specific atomic resonances, in the order of MHz-GHz, the uncertainty on the output of the device measuring the wavelength is often directly related to the final systematic uncertainty on the experimental results. Owing to its importance, the performance of several commercial wavelength meters was compared against different reference sources, including a Scanning Fabry-Pérot Interferometer (SFPI) and a frequency comb. Reproducible, wavelength- and device-dependent disagreements are observed, potentially skewing the experimental output at high precision. In this paper, a practical and relatively inexpensive wavelength meter characterization procedure is presented and validated. This method is capable of improving the precision on wavelength differences considerably depending on the device, while together with a second investigation that is published separately, [1], it offers a full description of the expected wavelength meter performance for users.

## I. INTRODUCTION

To run modern laser-spectroscopy experiments, the probe laser requires means to monitor, stabilize and/or scan the wavelength during operation. These tasks are often realized using state-of-the-art commercial wavelength meters, which are capable of performing a wavelength determination for a variety of optical radiation sources ranging from deep UV to infrared in relatively short time scales ( $> 1$  kHz), ideal for fast correction feedback loops. The performance of these wavelength meters has already been the topic of several studies, mainly focused on their performance stability (see e.g. [2–6]).

A specific field of use of these devices, is the study of exotic radionuclides at Radioactive Ion Beams (RIB) facilities via hyperfine laser spectroscopy. This technique provides information on the electromagnetic structure of the nucleus by offering a nuclear-model independent window to the nuclear spin, nuclear moments and differences in mean-square charge radii, for a range of isotopes [7, 8]. The hyperfine structure, carrying the nuclear information imprinted in the form of frequency differences between specific closely-spaced resonances in the atomic spectrum (MHz-GHz energy scale), can be uncovered with varying degrees of precision (defined here via the Full-Width-at-Half-Maximum (FWHM),  $\Delta f_{\text{FWHM}}$ , of the obtained resonance). As the production rate of nuclei decreases as

one pushes to more exotic species, Resonant Ionization Spectroscopy (RIS), whereby the number of ions produced as a function of laser wavelength is monitored, is the technique of choice due to the high efficiency of counting ions or detecting the radioactive decay signal. A number of RIS techniques exist, adapted to the environment in which the atomic species of interest are probed, which eventually defines the achievable precision [9]. These techniques are, for example: RIS in a hot-cavity source or in a gas cell ( $3 \text{ GHz} < \Delta f_{\text{FWHM}} < 10 \text{ GHz}$  [10, 11]), RIS in a perpendicular geometry, which can be realized in a gas jet or within the PI-LIST ion source ( $0.1 \text{ GHz} < \Delta f_{\text{FWHM}} < 1 \text{ GHz}$  [11, 12]) and with collinear techniques on fast ion/atom beams ( $\Delta f_{\text{FWHM}} \approx$  natural linewidth [13]). In order to reduce the linewidth of the hyperfine resonances, and, hence, to provide higher precision data on the nuclear observables, the latter two techniques are pushing the limits on accurate frequency determination by using commercial wavelength meters for monitoring, stabilizing and potentially scanning the probe laser [6].

As the final hyperfine observables of interest are directly related to the ill-defined uncertainty of the read-out of this wavelength meter, it is important to understand its performance in determining frequency differences  $\nu_{\alpha\beta} = \nu_{\beta} - \nu_{\alpha}$  of the order  $\sim$  MHz/GHz over the complete operational spectral range. Additionally, as the isotopes of interest are becoming increasingly exotic and, thus, only produced in minute quantities, the performance stability over longer periods of time, re-

\* Matthias.Verlinde@kuleuven.be

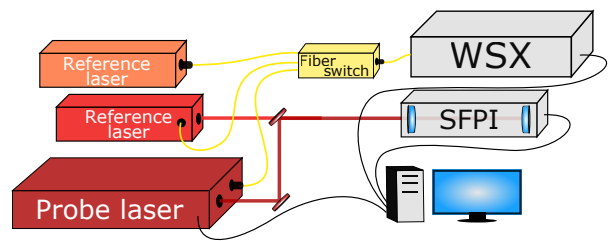
quired to obtain sufficient statistics, is crucial. Moreover, RIS most often relies on the measurement of one isotope at a time, so that the accurate determination of isotope shifts strongly depends on the comparability of the data and, thus, the reproducibility of the frequency determination. In this paper, we report on a reliability study performed in different laboratories using different wavelength ranges, different wavelength meters and different measuring protocols with the goal to provide an easy, cost-friendly, widely-applicable and potentially performance-increasing, wavelength meter characterization procedure. The wavelength meters of interest in this paper and [1] belong to the WS series from HighFinesse GmbH. These devices consist of beam optics coupling the laser light, entering the device via an optical fiber, into Fizeau interferometers. The induced interference pattern is imaged on a CCD photodiode array. The obtained spectrum is fitted and compared to the calibration pattern resulting in a wavelength determination. Here, we will concentrate on the accuracy of relative frequency measurements, while in a second study, the focus will lie on the accuracy of absolute frequency determinations [1].

To determine the precision on  $\nu_{\alpha\beta}$ ,  $\Delta\nu_{\alpha\beta}$ , for different wavelength meters in different wavelength ranges, the readout of these devices was compared to another reference. To summarize the tests, the paper is structured as follows. In Sec. II, the capabilities of several wavelength meters (WS series HighFinesse GmbH, when no specific type is specified the notation WSX is used) to accurately measure frequency differences,  $\nu_{\alpha\beta} = \nu_{\beta} - \nu_{\alpha}$ , in a range of  $\sim 10$  GHz is investigated with the aid of a Scanning Fabry-Pérot Interferometer (SFPI), a frequency comb and an ionic resonance. Sec. III contains a description of the temporal stability of these devices and different solutions on how to improve it. Several measurement methods are combined to give a comprehensive overview for a number of devices over a large spectral range. In Sec. IV, a validation of the results from Sec. II is done by performing laser spectroscopy on  $^{63,65}\text{Cu}$  isotopes in an Atomic-Beam Unit (ABU) and in a gas-jet environment, confirming the necessity of a proper wavelength meter characterization.

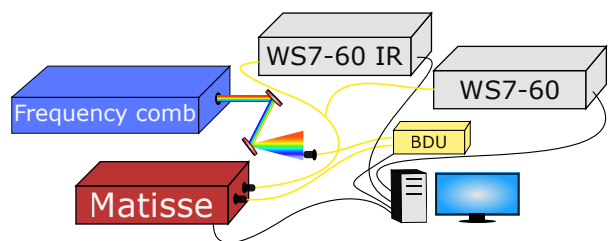
## II. DETERMINATION OF $\Delta\nu_{\alpha\beta}$ (WSX)

### A. WSX-SFPI comparison

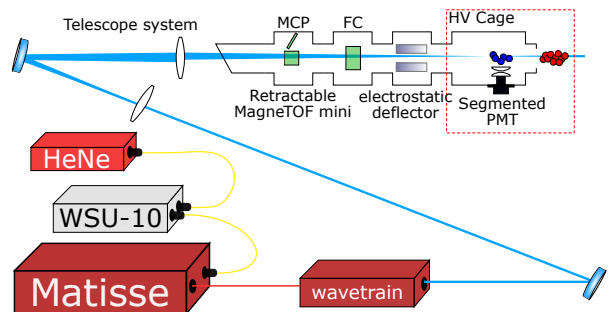
The first series of tests were performed at the In-Gas Laser and Ionization Spectroscopy (IGLIS) laboratory at KU Leuven, Belgium. This facility has been built to carry out a full characterization, validation and optimization of the in-gas-jet spectroscopy for its later implementation in a number of online accelerator facilities (S3 LEB, MARA LEB, GSI), to study, amongst others, the heavy and super heavy elements [11]. In the in-gas-jet method, the atoms of interest are embedded in a low-



(a) Simplified schematic layout of a general setup used to compare the output of an SFPI with that of a specific wavelength meter. The probe laser is measured by a specific WSX wavelength meter together with a reference laser. The wavelength scan of the probe laser is controlled externally by a feedback loop, based on the readout of the WSX. One reference laser is also overlapped with the probe laser and directed to the SFPI. For details, see text.



(b) Simplified schematic layout of the continuous wave (cw) laser setup at TU Darmstadt. The Matisse 2 TS laser frequency, locked to both reference cavity and FC1500 frequency comb, is monitored during a wavelength scan by the WS7-60 wavelength meters and by the comb itself via a Beat Detection Unit (BDU). For details, see text.



(c) Schematic view of the light collection region and laser systems of the collinear beamline at IGISOL for the measurements on  $^{89}\text{Y}$ . The ion beam enters the beamline from the right side. The laser interaction region is monitored by a segmented Photo-Multiplier Tube (PMT) for resonance fluorescence detection.

Figure 1: Experimental techniques used in this work.

density and low-temperature gas jet environment, minimizing the spectral pressure and temperature broadening mechanisms, while still offering high selectivity, short extraction time ( $< 0.5$  s), high efficiency and an indepen-

dence to the chemical nature of the species of interest [14]. To probe the hyperfine structure of the atoms embedded in the gas jet, high-repetition rate, high-power dye lasers are available, supported by a pulsed dye amplifier system seeded with a cw single-mode diode laser for high-resolution laser operation [15].

A second set of characterization tests were performed in the RISIKO laboratory at Johannes Gutenberg-University (JGU) Mainz, Germany. This facility is in use for studies on beams of stable or long-lived radioactive ions, in combination with related development on hot cavity laser ion sources, dedicated laser systems and spectroscopic techniques. The laser ion source here is based on high-repetition rate pulsed Ti:sapphire lasers specifically developed for this application [16]. While these lasers provide high output power required for efficient ionization, a complementary cw laser system provides the stability and narrow linewidth necessary for ultra-trace analysis applications [17, 18] and high-resolution spectroscopy [19–21]. The benefits of both systems can be combined by using a cw external cavity diode laser (ECDL) as master laser for seeding of a pulsed injection-locked Ti:sapphire laser (slave). This combination provides both, high-power pulsed laser radiation and a narrow spectral linewidth of  $\approx 20$  MHz with appropriate stability [22, 23], well suited for sensitive RIS studies.

#### *Measurement protocol*

The tests at the IGLIS laboratory were done by studying, simultaneously, the readout of a wavelength meter (WS7-60, acquired in 2012), which has a quoted accuracy of 60 MHz (according to the  $3\sigma$  criterion) in the range 420–1100 nm, and a Scanning Fabry-Pérot Interferometer (SFPI, Toptica FPI-100-0500-1) with a Free Spectral Range (FSR) of 4 GHz. A schematic overview of the setup is given in Fig. 1a. The IGLIS control software performs a stepwise frequency scan of a diode laser (TA:pro, TOPTICA Photonics AG) by applying a DC voltage to the DC 110 diode laser driver, a component of the Diode Laser Driver Electronics (Sys DC 110, TOPTICA Photonics AG), via a pulse generator (PicoScope 5000a, Pico Technology). This voltage is amplified in the DC110 diode laser driver and applied to a piezo actuator in the diode laser for accurate control of the laser wavelength. The TA:pro laser, lasing around 654.9 nm, is stabilized relative to the WS7-60's readout of either a 770.108796 nm diode reference laser (DL pro 780, TOPTICA Photonics AG), frequency locked to a potassium cell (CoSy, TEM Messtechnik GmbH), or a 632.991026 nm frequency-stabilized HeNe laser (Model 32734, Research Electro-Optics, Inc.) during a laser scan, see [15]. For the wavelength determination via the SFPI, both TA:pro and HeNe laser beams are overlapped in the SFPI. In this way, both wavelength measuring devices contain a reference source for calibration and stabilization purposes. A finesse,  $\mathcal{F} \approx 300$ , is obtained in

the SFPI for both TA:pro and HeNe laser light. To provide optimal working conditions for the SFPI, a scanning range of its piezo actuator is chosen such that a previously optimized number of fringes ( $\approx 10$ ) of both lasers is visible in one single voltage ramp. At each wavelength step of the TA:pro, one or more traces of the SFPI's diode sensor are recorded. Off-line, all data are analyzed with a Python-based algorithm. This program uses peak finder and peak tracker algorithms to identify HeNe and TA:pro fringes, fitting each with Gaussian profiles. The fringe positions of the HeNe laser are used as a ruler to accurately transform the time positions of each fringe into a frequency value via the known FSR. After this procedure the average position of the TA:pro fringes of each trace in the frequency domain is saved together with their standard deviation. In case higher precision is required, multiple traces can be extracted at each wavelength, providing a final value as the weighted average with corresponding uncertainty, taking into account the reduced  $\chi^2$ .

At the RISIKO laboratory, a similar comparison was performed between a wavelength meter (WSU-30, acquired in 2003) and a home made SFPI. The WSU-30(UV) wavelength meter has an accuracy of 30 MHz in the range 248–1180 nm. The scanning ECDL consists of a custom-built mount with a piezo-actuated grating for external feedback, and a Peltier element for temperature stabilization, supplied by commercial laser driver electronics (LDC202, Thorlabs Inc.). In total two different laser diodes were used in this setup (RWE-920, RWE-980, Eagleyard Photonics GmbH). Fast stabilization and scanning operation is performed with a quadrature interferometer, (iScan, TEM Messtechnik GmbH). The longterm and accurate stabilization of the ECDL set frequency is obtained from an SFPI via a fringe offset locking (FOL) technique [24]. More information on the laser setup can be found in [25]. Here, the light from the probe ECDL and from a stabilized HeNe laser (SL-03, SIOS Messtechnik GmbH) is overlapped in a custom-built confocal SFPI, with a piezo-actuated mirror. The SFPI has a free spectral range of  $\text{FSR} = 298.721$  MHz and a Finesse of  $\mathcal{F} \approx 400$ . Depending on the wavelength, the piezo ramp covers 2–3 fringes. The transmission of the probe ECDL and the HeNe fringes are separated by a dichroic mirror and detected with separate photodiodes. The time difference of the first ECDL fringe after the start of the voltage ramp is measured with respect to the fringe from the reference HeNe laser via a counter card and the frequency change is evaluated using an Arduino MCU, via the precisely known FSR and HeNe wavelengths. To ensure proper single-mode operation of the ECDL, the time between the first and the second fringe is in addition evaluated. Values of the mean relative frequency and frequency jitter within a time of  $\approx 50$  ms (matched to the data acquisition cycle of the wavelength meter) are sent to a LabVIEW interface, used for controlling, monitoring and recording. An absolute frequency measurement is provided by the WSU-30,

where both the probe ECDL and the stable HeNe output are measured through a multichannel switch (High-Finesse GmbH). The absolute reference and calibration source for the wavelength meter is an additional ECDL (DL pro 780, Toptica Photonics AG), coupled to a compact rubidium saturated absorption spectroscopy setup (SAS) (CoSy 4.0, TEM Messtechnik GmbH). By using a dither-lock stabilization (LaseLock 3.0, TEM Messtechnik GmbH), it is locked to the  $F = 2 \rightarrow F = 3$  transition in the D2 line of  $^{87}\text{Rb}$  at 780.24602 nm. A schematic overview of this setup is shown in fig. 1a.

To compare the relative performance of both SFPI and wavelength meter during a frequency scan, the magnitude of each laser step with respect to the starting point of the scan is monitored for both devices. Finally, the difference in the step size as measured by the SFPI and wavelength meter, respectively, is subtracted to obtain a relative result. Mathematically, the final output  $\Delta_{\text{SFPI-WSX}}(\nu)$  for a random wavelength meter WSX, reads as follows:

$$\begin{aligned} \Delta_{\text{SFPI-WSX}}(\nu) &= \Delta_{\text{SFPI}}(\nu) - \Delta_{\text{WSX}}(\nu) \\ &= (\nu_{\text{SFPI}} - \nu_{0,\text{SFPI}}) - (\nu_{\text{WSX}} - \nu_{0,\text{WSX}}). \end{aligned} \quad (1)$$

In Eq. (1),  $\nu_{\text{WSX}}$  represents the frequency readout at a certain moment during a laser scan while  $\nu_{0,\text{WSX}}$  represents a reference point within the scan.

### Results

The procedure described for the IGLIS laboratory, using the setup in Fig. 1a, was applied to a number of scan ranges. The results for  $\Delta_{\text{SFPI-WS7}}(\nu)$ , defined in Eq. (1), in the 654.9570-654.9969 nm range (spanning roughly 28 GHz in total) are shown in Fig. 2. These results show that the WS7-60 and SFPI disagree reproducibly on the step size taken by the TA:pro laser with a maximum of 8 MHz, with an additional degree of periodicity. To map this periodicity, a triangular wave form was fitted to the data of Fig. 2 without any prior knowledge on the underlying mechanism:

$$\begin{aligned} \Delta_{\text{triangle}}(\nu) &= \frac{4A}{T} \left( (\nu + S) - \frac{T}{2} \left[ \frac{2(\nu + S)}{T} + \frac{1}{2} \right] \right) \\ &\cdot (-1)^{\lfloor \frac{2(\nu + S)}{T} + \frac{1}{2} \rfloor}. \end{aligned} \quad (2)$$

This function of the frequency  $\nu$  has three parameters; the amplitude,  $A$ , period,  $T$  and shift,  $S$ , of the triangular wave. The fitting procedure reveals a peak-to-peak amplitude  $A_{655}^{\text{WS7}} = 8.2(2)$  MHz and a period  $T_{655}^{\text{WS7}} = 3.871(10)$  GHz for Eq. (2). The period matches closely to the FSR of the most precise interferometer of the WS7-60 wavelength meter ( $\approx 4$  GHz). To understand the behavior of the WS7-60 in more detail, the wavelength range 654.973-654.985 nm was scanned with higher resolution ( $\approx 10$  traces per wavelength

step were combined). The results of this measurement are shown in yellow in Fig. 2 with a magnified region shown in Sec. IV, Fig. 10. The finer details observed in Fig. 10 shows that the underlying mechanism, causing the disagreement between the WS7-60 and SFPI, is of a more complex nature than a simple triangular waveform. However, the general features of the disagreement between both devices are clear. The data of Fig. 2 present multiple measurements confirming the reproducibility of the results. Additionally, the structure obtained for Fig. 2 is independent of the calibration laser. The specific calibration tool only causes an absolute offset, not visible in these measurements.

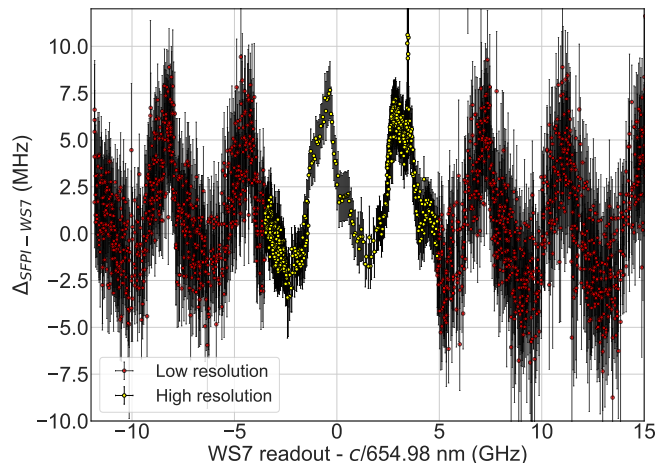


Figure 2: The results for  $\Delta_{\text{SFPI-WS7}}(\nu)$ , defined in Eq. (1), recorded at the IGLIS laboratory. The results presented here combine multiple scans taken at different times to prove the reproducibility of the data. For details, see text.  $c$  presents the speed of light in m/s.

The comparison between the WSU-30 wavelength meter and the home made SFPI at the RISIKO laboratory is presented in Fig. 3 (middle and bottom panel). The data in Fig. 3 shows also a periodic deviation of the WSU-30 readout with respect to the SFPI, calculated according to Eq. (1), with  $\nu_{0,\text{WSU30}} = c/905.795$  nm and  $\nu_{0,\text{WSU30}} = c/938.853$  nm for middle and lower graph, respectively ( $\nu_{0,\text{SFPI}} = 0$ ). In both measurements a calibration of the wavelength meter was performed after each data point, to exclude any time-dependent drifts of the wavelength meter performance, as discussed in the next section. The rather large scatter in the scan at 905 nm arises from stability issues of the probe ECDL, which may be caused by internal feedback in the laser diode, owing to an inferior anti-reflection coating of the front window. The different colors represent measurements performed on different days over the same frequency range and underline the reproducibility of the periodic pattern. Minor shifts may be caused by drifts of the HeNe laser (i.e. the SFPI reference), but still lie within the specified stability. Fitting all datapoints of one frequency range with the tri-

angular pattern from Eq. (2) yields a period of  $T_{905}^{\text{WSU30}} = 1.923(14)$  GHz and  $T_{938}^{\text{WSU30}} = 1.912(12)$  GHz, close to the FSR of the final WSU-30 interferometer of  $\approx 2$  GHz. The peak-to-peak deviation is  $A_{905}^{\text{WSU30}} = 5.1(3)$  MHz and  $A_{938}^{\text{WSU30}} = 5.3(2)$  MHz, respectively. To confirm both the IGLIS and RISIKO data acquisition and in general the SFPI measurement procedure, the WSU-30 wavelength meter was remeasured at the IGLIS laboratory in the wavelength range around 654.980 nm. The results are shown in Fig. 3 (top panel) and they confirm both the  $\approx 2$  GHz period for this WSU-30 and the smaller amplitude compared to the WS7-60 ( $A_{655}^{\text{WSU30}} \approx 5$  MHz). While the 'global' periodicity of the signal is easily distinguished, extra structures are clearly visible. The obtained results for  $\Delta_{\text{SFPI-WSU30}}$ , also, clearly show both a wavelength range and device-specific dependency of the wavelength meter response, as was confirmed in the next measurements.

### B. WSX-frequency comb comparison

A third series of wavelength meter tests was performed at the Collinear Apparatus for Laser spectroscopy and Applied physics (COALA) at TU Darmstadt, Germany. This laboratory was originally designed for accurate high-voltage evaluations based on Collinear Laser Spectroscopy (CLS) operation. Nowadays, precise measurements of absolute transition frequencies and isotope shifts in ions are also performed to benchmark atomic theory and to support on-line investigations of short-lived isotopes. For this purpose, a cw laser system based on Ti:sapphire lasers combined with Wavetrain frequency doublers is available alongside a GPS-referenced frequency comb to determine and stabilize its frequency [1, 26, 27].

#### *Measurement protocol*

At the COALA laboratory the output of both the IGLIS WS7-60 wavelength meter and the in-house WS7-60-IR (630-1750 nm, acquired in 2007) device was compared to the frequency comb (FC1500-250-WG, Menlo Systems) and the accuracy of the wavelength meter's absolute readout could be tested. The setup is shown in Fig. 1b. A Ti:sapphire laser (Matisse 2 TS, Sirah) is stabilized to its reference cavity to avoid short-term frequency fluctuations. Additionally, a slower stabilization feedback loop for long-term stabilization is realized using the frequency comb. To achieve this, the beat frequency between the nearest comb mode and the Ti:sapphire beam is measured in a fiber-coupled beat detection unit (BDU) and digitally communicated to the Matisse commander software, which adapts the length of the reference cavity to keep the beat frequency constant. In this way, an accurate and stable absolute reference is available with a precision of better than 100 kHz, limited by the linewidth

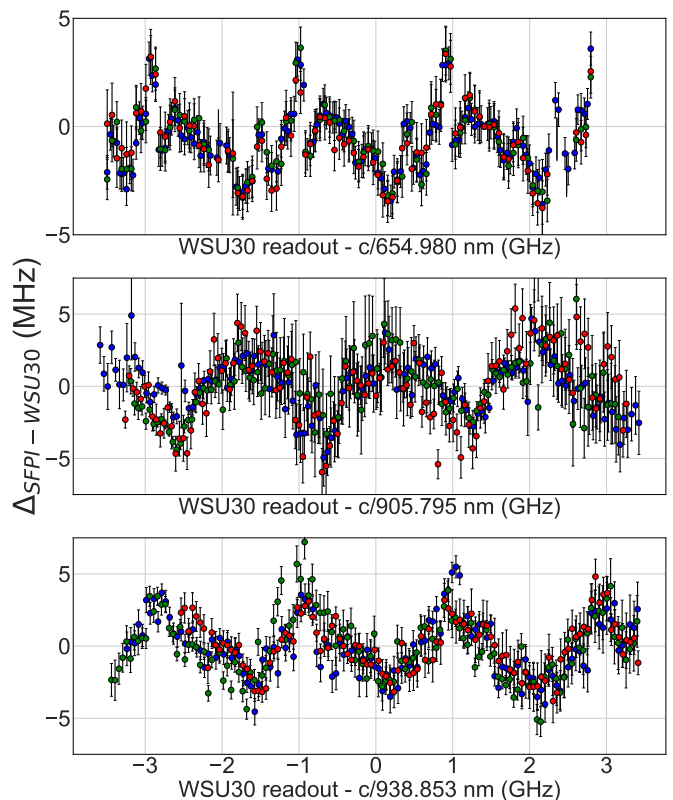


Figure 3: Results for  $\Delta_{\text{SFPI-WSU30}}$ , measured for three different laser wavelength ranges. The upper panel at 654.980 nm was obtained at the IGLIS laboratory. Each data point of the upper panel is taken as the weighted average with corresponding uncertainty of the results from 10 SFPI traces, obtained via Eq. (1), at a distinct frequency. Around 10 consistent measurements were taken, from which three are shown in the upper panel.

The other panels, scanned at 905.795 nm and 938.853 nm, respectively, were measured at the RISIKO laboratory in Mainz. The results are obtained with a similar analysis to the one in the IGLIS laboratory, and the final data points represent the average and standard deviation of all SFPI results taken within one wavelength bin. 11 and 8 consistent measurements were taken for the 905 nm and 938 nm cases, respectively, from which again three full range results are shown in both panels. All three measurements for  $\Delta_{\text{SFPI-WSU30}}$  show the same period in their structure.

of the Matisse. For the measurements performed here, the laser is scanned across a similar frequency range as in the IGLIS/RISIKO measurements, locked to the frequency comb at every wavelength step. The customized data acquisition system records the readout from both the frequency comb and the two WS7-60 wavelength meters. With this setup, both relative and absolute performance of the WS7-60 can be mapped across a large wavelength range.

As the combination of the frequency comb and the Ma-



tisse laser at the COALA laboratory offers a reference with a well-known frequency, one can go a step further than Eq. (1) and compare directly the frequency output of both devices:

$$\Delta_{\text{Comb-WSX}}(\nu) = \nu_{\text{Comb}} - \nu_{\text{WSX}}. \quad (3)$$

In this case, the wavelength meters are not only tested in their ability to determine  $\nu_{\alpha\beta}$  but also in measuring  $\nu_{\alpha}$  itself.

### Results

The results for the comparison between the WS7-60 and WS7-60-IR wavelength meters and the FC-1500 frequency comb, performed at the COALA laboratory, are shown in Fig. 4. They are obtained from a scan of the Matisse laser across  $\approx 16$  GHz around 805.56 nm and 795.56 nm, and across  $\approx 8$  GHz around 856.45 nm, respectively. The wavelength meters are calibrated at 812.77 nm using the frequency-comb stabilized Matisse, for the measurements at 805 nm and 856 nm and at 632.99 nm with a frequency-stabilized HeNe laser (SIOS SL 03, Meßtechnik GmbH) for the measurement at 795.56 nm. To identify device-dependent effects, a WS7-60-IR was included in the measurements. From Fig. 4, it follows that similar periodic patterns arise at different wavelength ranges, with similar peak-to-peak discrepancies for both wavelength meters. The structure is found to be highly reproducible over months in previous measurements performed at COALA [1]. Inspecting both Figs. 2 and 4 indicates a wavelength dependence of the discrepancy between the reference and the WS7-60. Additionally, both devices do not react in the same way, indicating an additional device-dependent effect on the results of  $\Delta_{\text{Comb-WS7}}(\nu)$ . Finally, it should be mentioned that the structure in the results of Fig. 4 also does not depend on the specific calibration point of the laser. Only the absolute offset to the real wavelength determined with the frequency comb might change, which is strongly wavelength-dependent itself. This as well as a full description of the frequency-comb based specification of various high-precision wavelength meters is presented in [1].

### C. WSX-ionic resonance comparison

A final series of measurements was done at the IGISOL facility of the Accelerator Laboratory in the University of Jyväskylä, Finland. This facility uses the ion guide technique for the production and study of low-energy beams of exotic radioactive nuclei [28]. Fundamental nuclear ground and isomeric state properties and mass are probed using a variety of ion (and atom) manipulation devices including ion traps, radiofrequency (rf) cooler-bunchers as well as methods of optical spectroscopy.

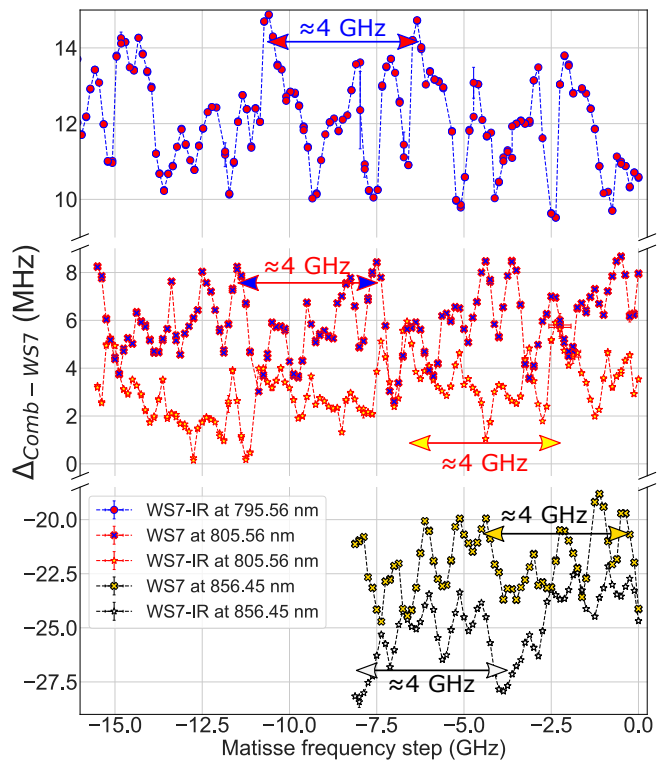


Figure 4: Benchmarking the performance of two different WS7-60 devices, in the vicinity of 805.56 nm, 856.45 nm, and 795.56 nm against a frequency-comb measurement of the laser frequency resulting in  $\Delta_{\text{Comb-WS7}}(\nu)$ .

Over the years an expanding program of optical spectroscopy at the facility has resulted in a variety of improvements to methods including collinear laser spectroscopy as well as resonance ionization spectroscopy. The former technique is applied for high-resolution spectroscopy on fast ionic and atomic beams, routinely providing measurements of optical frequency splittings to 1-10 MHz precision. For these applications, a high-resolution laser spectroscopy setup based on a Matisse 2 TS laser and a Wavetrain frequency doubler, is available. Additional infrastructure includes an injection-locked Ti:sapphire laser, seeded by the Matisse cw light, and several wavelength reference options.

### Measurement protocol

At the IGISOL facility beam line for collinear laser spectroscopy, a wavelength meter (WSU-10, acquired in 2017), with a specified 10 MHz accuracy, was investigated. A schematic of the laser system and light collection region of the collinear beam line can be seen in Fig. 1c. More details on the beamline and data acquisition system can be found in [29]. Stable  $^{89}\text{Y}$ , pro-

duced by a spark discharge source, was measured on the 363.4157 nm transition from the ionic ground state using the Matisse TS laser, pumped by a cw frequency doubled YAG-laser (Millenia eV, Spectra Physics) and stabilized to a fixed setpoint in the wavelength meter. Resonant interaction between the anti-collinear laser beam and ions is measured by monitoring the optical deexcitation of the excited state with a segmented Photo Multiplier Tube (PMT). The hyperfine structure can be mapped by tuning the acceleration voltage of the ion beam. To probe systematic discrepancies between the WSU-10 and the centroid of the 363.4157 nm transition used as a reference, the stabilization setpoint was changed in steps of 600 MHz, and for each setpoint a spectrum with sufficient statistics ( $> 1000$  counts on the resonance peak) was collected.

For the IGISOL wavelength meter tests, the centroid of  $^{89}\text{Y}$  presents an absolute reference while it is assumed that the voltage scan is identical for every measurement. This results in:

$$\Delta_{\text{Centroid}}(\nu) = (V_{\text{Centroid},\nu} - V_{\text{Centroid},\nu_0}) \frac{\partial\nu}{\partial V}. \quad (4)$$

Here  $V_{\text{Centroid},\nu}$  is the voltage at which the centroid of the transition is obtained for a random measurement at fixed setpoint  $\nu$  and  $V_{\text{Centroid},\nu_0}$  is the same for a reference measurement.  $\partial\nu/\partial V$  converts the acceleration voltage difference to a frequency difference via the Doppler shift. In this way, similar results are obtained as for Eq. (1) and Eq. (3).

### Results

The resulting  $^{89}\text{Y}$  hyperfine spectrum consists of an unresolved doublet, which was fitted by fixing the hyperfine parameter of the upper state to the literature value of 32.6(1) MHz [30]. The fitted centroid frequencies of the 363.4157 nm transition, obtained from the collinear beam line at IGISOL, are depicted in Fig. 5. A triangular wave pattern applied to the data, following Eq. (2), resulted in a peak-to-peak amplitude of  $A_{727}^{\text{WSU}10} = 1.3(3)$  MHz, which is almost an order of magnitude smaller than for the WS7-60. The period  $T_{727}^{\text{WSU}10} = 1.99(12)$  GHz, is consistent with the  $\approx 2$  GHz FSR of the most precise interferometer in the wavelength meter.

### D. Summary

In summary, the results indicate that each wavelength meter has its characteristic  $\Delta\nu_{\alpha\beta}$  that is unique for every instrument separately. It can be extracted from  $\Delta_{\text{SFPI-WSX}}(\nu)$ ,  $\Delta_{\text{Comb-WSX}}(\nu)$  and  $\Delta_{\text{Centroid}}(\nu)$ , depends on the wavelength range of interest and is characterized by a periodic structure which follows the FSR

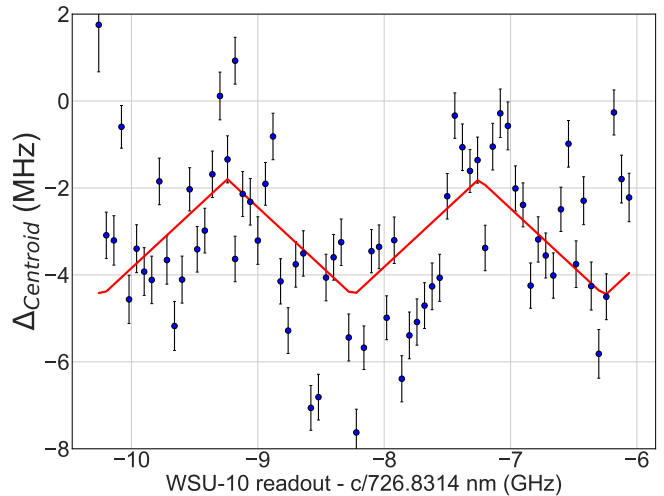


Figure 5: The fitted centroid of the  $^{89}\text{Y}$  hyperfine structure at changing laser stabilization setpoints using the WSU-10 wavelength meter (blue). The resulting data has been fitted using a triangular wave function according to Eq. (2) (red solid line).

of the most precise interferometer in the device. To obtain a value for  $\Delta\nu_{\alpha\beta}$ , one should perform a characterization procedure as presented here and further elaborated on in Sec. IV, or otherwise remain with the conservative absolute accuracy mentioned by the manufacturer. To assess the potential systematic uncertainty to be expected, our data is summarized in Table I, which contains the  $A_{\lambda}^{\text{WSX}}$  alongside the outer boundaries of the  $\Delta_{\text{SFPI-WSX}}(\nu)$ ,  $\Delta_{\text{Comb-WSX}}(\nu)$  and  $\Delta_{\text{Centroid}}(\nu)$  distributions covering 95% or 99.7% of all measurements.

### III. TEMPORAL STABILITY OF $\nu_{\alpha}(\text{WSX})$

Following a comparison of the performance of different wavelength meters in determining  $\nu_{\alpha\beta}$  in a range of  $\sim 10$  GHz with that of an SFPI and a frequency comb, its stability over time is mapped. A well-known feature of these wavelength meters is their tendency to drift over longer periods of time, strongly correlated to external temperature and/or pressure instabilities. The magnitude of these drifts is most often in the range of a few MHz/hour dependent on the magnitude of the time derivative of the external conditions. During longer measurement times, these drifts will have a profound impact on the results obtained. Two options exist to compensate for the time-dependent readout of the wavelength. First of all, one can correct for the drift of the scanning laser by monitoring the wavelength of an externally locked reference laser at the same time, which will be discussed in Sec. III A. Secondly, a periodical calibration of the wavelength meter can be included in the control software of the laser, see Sec. III B.

To exemplify the importance of a well-controlled external



Wavelength meter	Wavelength probe (nm) [ $\pm 5 - 20$ GHz]	$A_\lambda^{\text{WSX}}$ MHz	$Q_{95}$ (MHz)	$Q_{99.7}$ (MHz)
WS7-60	655.0	8.2(2)	11.7	18.0
WS7-60	856.5	$\approx 3.5$	5.0	5.9
WS7-60	805.6	$\approx 5$	5.1	6.1
WS7-60-IR	856.5	$\approx 4$	5.7	6.2
WS7-60-IR	805.6	$\approx 3.5$	4.7	5.8
WS7-60-IR	795.6	$\approx 5$	4.5	5.4
WSU-30	655.0	$\approx 5$	6.4	7.3
WSU-30	905.8	5.1(3)	8.8	13.7
WSU-30	938.9	5.3(2)	7.2	11.6
WSU-10	726.8	1.3(3)	7.2	9.2

Table I: The peak-to-peak amplitude  $A_\lambda^{\text{WSX}}$  and outer boundaries of the  $\Delta_{\text{SFPI-WSX}}(\nu)$ ,  $\Delta_{\text{Comb-WSX}}(\nu)$  and  $\Delta_{\text{Centroid}}(\nu)$  distributions, covering 95% or 99.7% of all measurements performed,  $Q_{95}$  and  $Q_{99.7}$ . When no explicit correction to the wavelength meter output is applied, see Sec. IV,  $Q_{95}$  and  $Q_{99.7}$  should be taken into account to determine the systematic uncertainty on a determination of  $\Delta\nu_{\alpha\beta}$  in a specific wavelength range. The Q values are not only influenced by the wavelength meter but also by the uncertainty of the analysis procedure. The values of  $A_\lambda^{\text{WSX}}$  are approximated in case the discrepancy of the wavelength meter shows significant deviation from Eq. (2).

environment on the wavelength meter’s long-term performance, the Matisse 2 TS laser at IGISOL was stabilized to a Rb hyperfine peak using a side-of-fringe stabilization method implemented in LabVIEW while being monitored by the WSU-10. Any wavelength meter drifts are then transferred to the device’s readout. The largest variation seen is approximately 4 MHz over 24 hours. This stability is in part due to the stable laboratory environment, with laboratory temperature control and minimal disturbance. To account for larger drifts in less stable conditions, they can be corrected for by (auto-)calibrating the device to a frequency-stabilized HeNe laser at certain times suitable to the ongoing measurements, see Sec. III B. Because the high resolution work at the collinear beam line of IGISOL is performed with a fixed laser frequency setpoint, the Matisse transfer cavity can be used to bypass the wavelength meter in general. In this case, a digital plugin of the Matisse control software uses the intensity of the HeNe (HRS015B, Thorlabs Inc.) measured behind the reference cell with a photodiode (PDA36A-EC, Thorlabs Inc.) to stabilize the reference cell length with the side-of-fringe locking method. In this manner, the absolute frequency stability is now directly related to the frequency stability of the HeNe laser, eliminating the need for the wavelength meter. Collinear laser spectroscopy on stable even-even ytterbium isotopes was performed using either the wavelength meter or the transfer cavity for frequency stabilization to verify proper functioning of the transfer cavity. The scatter on the fitted centroids for each isotope, measured in the course of a few hours, was reduced when stabilized to the transfer cavity compared to the wavelength meter, confirming the wavelength meter as a possible source of systematic uncertainty, see Fig. 6.

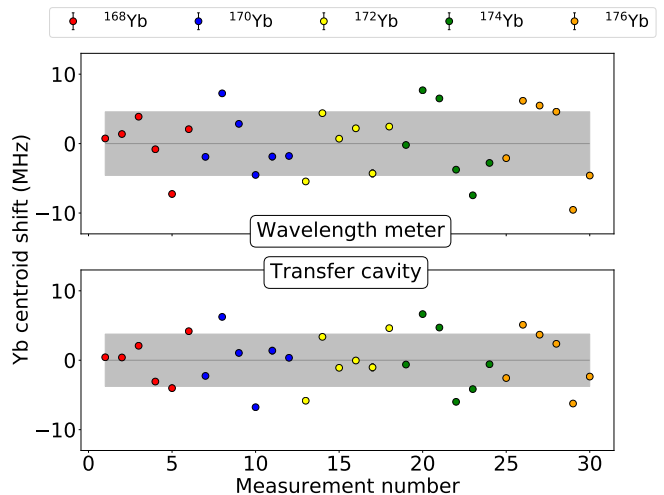


Figure 6: Scatter of the  $^{168}\text{Yb}$ ,  $^{170}\text{Yb}$ ,  $^{172}\text{Yb}$ ,  $^{174}\text{Yb}$  and  $^{176}\text{Yb}$  centroids, obtained through collinear laser spectroscopy for different measurements stabilizing the probe laser to either the WSU-10 wavelength meter or the Matisse 2 TS transfer cavity. All centroids of a specific isotope, which were measured with a total of 6 different laser setpoints, are compared to their average. The  $1\sigma$  confidence level was reduced from 4.6 MHz to 3.8 MHz when stabilization to the transfer cavity was done.

### A. Drift correction

The most general correction to drifts in the wavelength meter output, in the presence of a reference laser, can be written as follows:

$$\nu'_{\text{corr,WSX}} = \nu_{\text{set}} + \beta(\nu_{\text{set}}, \nu_{\text{ref}}, t)(\nu_{\text{ref}} - \nu_{\text{ref,WSX}}). \quad (5)$$

$\nu_{\text{set}}$  is the originally defined setpoint at which the laser should be stabilized,  $\nu_{\text{ref}}$  represents the absolute frequency of the reference laser and  $\nu_{\text{ref,WSX}}$  is the reference's wavelength meter readout. The parameter  $\beta(\nu_{\text{set}}, \nu_{\text{ref}}, t)$  takes into account any kind of frequency and/or time-dependent differences between the drift of the reference laser and the probe laser. As outlined in [15], the IGLIS control software stabilizes the scanning TA:pro's frequency at a wavelength  $\nu'_{\text{set,WS7}}$  in the WS7-60, with  $\beta(\nu_{\text{set}}, \nu_{\text{ref}}, t) = 1$ . Doing so, wavelength meter dependent drifts in time, which can be as large as 5 MHz/h for the WS7-60 of interest, are corrected. To identify higher order (wavelength and/or time-dependent) corrections to  $\nu'_{\text{set,WS7}}$  in the form of

$$\beta(\nu_{\text{set}}, \nu_{\text{ref}}, t) = \frac{\nu'_{\text{set,WS7}} - \nu_{\text{set}}}{\nu_{\text{ref}} - \nu_{\text{ref,WS7}}}$$
, three independent measurements were done both at the IGLIS laboratory, a temperature-controlled ( $\pm 0.5$  °C) ISO8 clean room, and the COALA laboratory (see Figs. 7a to 7c). In all three cases, a HeNe laser was used both to calibrate the wavelength meter and as reference for the correction applied as it is the most common reference source. In addition to the HeNe, another externally stabilized laser, a proxy for the laser to be monitored during the experiment, was read out by the WS7-60 to search for any frequency dependence in  $\beta(\nu_{\text{set}}, \nu_{\text{ref}}, t)$ . First, the IGLIS TA:pro, stabilized to the wavelength meter readout at 654.97538 nm was included. Secondly, a potassium-locked diode was used at 770.10878 nm, also at the IGLIS laboratory. Finally, a Matisse 2 TS Ti:sapphire laser, locked to the FC1500 frequency comb at the COALA laboratory, was monitored at a wavelength of 787.82884 nm. The drift of the TA:pro was measured by supplying the laser, stabilized to  $\nu_{\text{set}}$  in the WS7-60, also to the SFPI. The data analysis of these results remains the same as described in Sec. II B. For all three measurements, the full drift of the WS7-60's response in  $\approx 6$  h is mapped together with the results of available corrections. These corrections include  $\beta(\nu_{\text{set}}, \nu_{\text{ref}}, t) = 0$ ,  $\beta(\nu_{\text{set}}, \nu_{\text{ref}}, t) = 1$  and  $\beta(\nu_{\text{set}}, \nu_{\text{ref}}, t) = \beta(\nu_{\text{set}}, \nu_{\text{ref}})$ . The factor  $\beta(\nu_{\text{set}}, \nu_{\text{ref}})$  is a reproducible, wavelength-dependent constant, which is obtained after longer periods of drift as can be seen in Figs. 7a to 7c. This number is reproducible for different measurements, independent of the drift rate, showing only a dependence on the device,  $\nu_{\text{set}}$  and  $\nu_{\text{ref}}$ . From the data, one can see that the WS7-60 does not provide a stable read out of the wavelength over time (this would be the case  $\beta(\nu_{\text{set}}, \nu_{\text{ref}}, t) = 0$ ). For the TA:pro at 654.98 nm,  $\beta(\nu_{\text{set}}, \nu_{\text{ref}}, t) = 1$  is sufficiently accurate to keep the laser stable to within 1 MHz. This 1 MHz limit was chosen arbitrarily as it is similar to other uncertainties contributing to the laser stability, as will be discussed in Sec. IV. For both infrared lasers, the inclusion of the  $\beta(\nu_{\text{set}}, \nu_{\text{ref}})$  factor is required to ensure a similar stability over this time domain. Through these measurements, it can be concluded that a correction to the WS7-60 output with  $\beta(\nu_{\text{set}}, \nu_{\text{ref}}, t) = 1$ , is sufficient up to scan times of  $\approx 30$  min. For longer scans, either the  $\beta(\nu_{\text{set}}, \nu_{\text{ref}})$  factor

has to be determined and applied, or a recalibration is required with a repetition rate higher than once every  $\approx 30$  min, as will be discussed next.

## B. Periodical calibration

The stability of the WSU-30 wavelength meter readout at the RISIKO laboratory was tested over a period of  $\approx 1$  day by monitoring the measured frequencies of the Rb-locked ECDL and the HeNe after one initial calibration to the Rb D2 line. In a second measurement, one day later, the wavelength meter was auto-calibrated to the Rb-locked ECDL with a cycle of 10 minutes. The results are presented in Fig. 8. It can be clearly seen that without auto-calibration (AC), the wavelength meter readout drifts over a few tens of MHz, strongly correlated to the temperature. Moreover, at large deviations from the nominal frequency, the HeNe readout seems to drift further than the Rb-locked ECDL, indicating also here  $\beta(\nu_{\text{set}}, \nu_{\text{ref}}, t) \neq 1$ .

Auto-calibration resolves the long-term stability issues of the wavelength meter readout almost completely. The deviation  $\nu - \nu_{\text{cal}}$  to the calibration frequency is  $< 2$  MHz over the measurement duration and can be further reduced by a shorter calibration interval. As a consequence an AC routine was added to the data acquisition cycle, so that the wavelength meter can be calibrated (taking less than 1 s) before moving to the next frequency setpoint. Alternatively, a stable temperature environment for the wavelength meter should provide superior frequency stability than in our test without AC. In this case one should also consider the air pressure in the room, which could not be measured with our device. Newer devices usually have an integrated pressure sensor.

## IV. VALIDATION

The reliability of the laser system in general and the WS7-60 wavelength meter in particular was tested by performing hyperfine spectroscopy on the  $4s\ ^2S_{1/2}$  ground state (g.s.) to the  $4p\ ^2P_{1/2}$  excited state (e.s.) transition in  $^{63,65}\text{Cu}$ , in an Atomic-Beam Unit (ABU) and in a gas jet, and comparing the results with literature. The resulting data as well as the excitation and ionization scheme are presented in Fig. 10. To achieve the excitation at 327.49 nm, light from the scanning TA:pro laser is amplified in a Pulsed Dye Amplifier (PDA, Sirah Lasertechnik GmbH) and frequency doubled in a BBO nonlinear crystal. The ionization step of 287.98 nm is provided by a broadband tunable dye laser (CREDO, Sirah Lasertechnik GmbH) with also an integrated frequency conversion unit. Both PDA and broadband dye lasers are pumped by Nd:YAG lasers (INNOSLAB, Edgewave GmbH) at 1 kHz with a pulse length of  $\approx 7$  ns. The ABU provides a copper atom plume by resistively heating a graphite tube filled with copper. After ionization, these atoms experi-

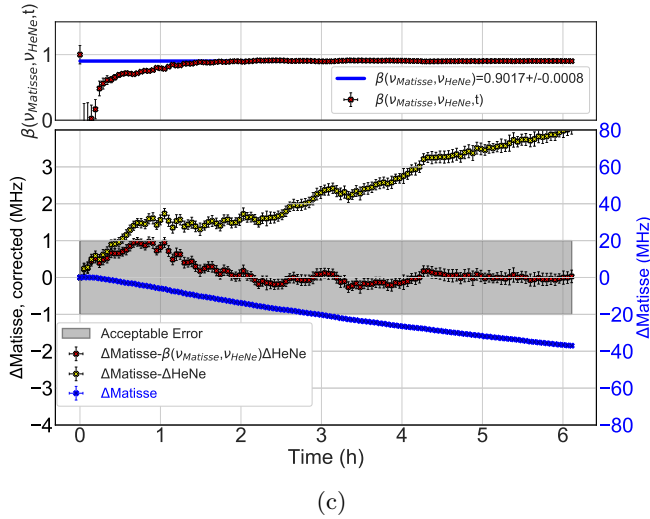
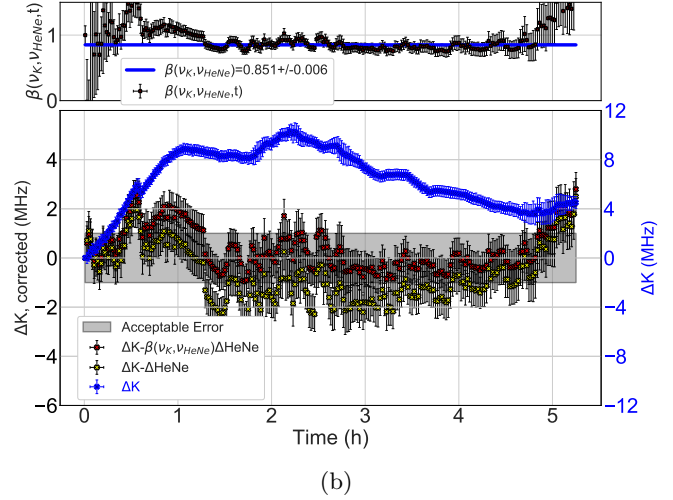
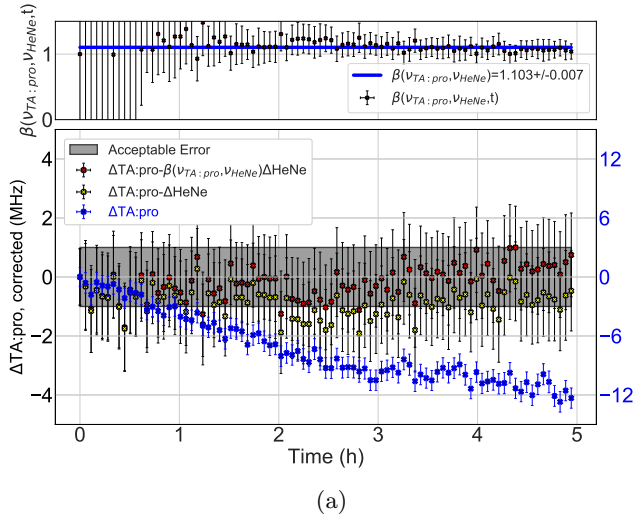


Figure 7: The time dependence of the WS7-60's response to an externally locked laser at 654.97538 nm (Fig. 7a), 770.10878 nm (Fig. 7b) and 787.82884 nm (Fig. 7c), respectively. The drift is defined as  $\Delta X = \nu_{WS7}(t) - \nu_{WS7}(t_0)$ , with  $t_0$  being the time of calibration and  $X$  the specific laser used. The uncorrected readout (right axis, blue) is plotted alongside possible corrections (left axis, yellow for  $\beta(\nu_{set}, \nu_{ref}, t) = 1$  and red for  $\beta(\nu_{set}, \nu_{ref}, t) = \beta(\nu_{set}, \nu_{ref})$ ), see text for details. The measured correction factor  $\beta(\nu_{set}, \nu_{ref}, t)$ , with its stable value,  $\beta(\nu_{set}, \nu_{ref})$ , fitted to the data, is added to the top panel of each figure. The different drift amplitudes originate from differences in the external conditions during the measurement.

ence a two-stage acceleration region before a field free drift towards a Multi Channel Plate (MCP) detector. At the MCP, the time-of-flight of copper ions is recorded to provide a mass resolving power of  $R \approx 150$  for  $^{63}\text{Cu}$ . For the gas jet, copper atoms are produced by resistively heating a copper filament inside a buffer gas cell filled with argon. After laser ionization in the jet formed by a de Laval nozzle, placed at the gas-cell exit, these ions are transported through a set of Radio-Frequency Quadrupoles (RFQ's) and ion optical elements to a dipole magnet mass separator ( $R \approx 300$ ) on high voltage. The mass-separated ions are finally detected by an MCP. More details on the setup system is available in [15, 31]. A schematic overview of the laser setup for an ABU measurement is shown in Fig. 9. The scheme for in-gas-jet measurements is similar with the exception that the laser beams are sent to the adjacent separator lab for overlap in the gas jet. An example of the resulting hyperfine structure, obtained from an ABU measurement, is visualized in the bottom part of Fig. 10. The measuring protocol, automatized in the IGLIS Control Software and outlined in [15] provides, together

with additional systematic checks, all data required to specify the expected uncertainties on both the ion rate and wavelength determination. The uncertainty on the ion arrival rate,  $I$ , is deduced from the standard deviation of a number of measurements,  $I \pm \Delta I = \langle I \rangle \pm \sqrt{\langle I^2 \rangle - \langle I \rangle^2}$ , at a specific wavelength,. The uncertainty on the wavelength  $\nu$  comprises of several components  $\Delta\nu_{stat}, \Delta\nu_{stab}, \Delta\nu_{drift}, \Delta\nu_{corr}$ , combining to  $\nu_\alpha \pm \Delta\nu_\alpha = \langle \nu \rangle \pm \sqrt{(\Delta\nu_{stat})^2 + (\Delta\nu_{stab})^2 + (\Delta\nu_{drift})^2 + (\Delta\nu_{corr})^2}$ . Here,  $\Delta\nu_{stat}$  represents the standard deviation of all wavelength values read out by the WS7-60 in a specific wavelength step, typically  $\Delta\nu_{stat} \approx 1$  MHz, see [15].  $\Delta\nu_{stab}$  covers the stability of the frequency reference,  $\approx 1$  MHz in one hour for the HeNe and  $< 1$  MHz for the potassium-locked diode laser. Third,  $\Delta\nu_{drift}$  describes the uncertainty on the WS7-60's drift correction. For the IGLIS control software,  $\beta(\nu_{set}, \nu_{ref}, t) = 1$ . In this case,  $\Delta\nu_{drift}$  remains  $< 1$  MHz for a scan at 654.98 nm, see Fig. 7a. Finally,  $\Delta\nu_{corr}$  can be added to account for any applied corrections to the WS7-60 output. Within these specifications, a multitude of scans are performed in high resolution mode in the ABU. For each scan, a

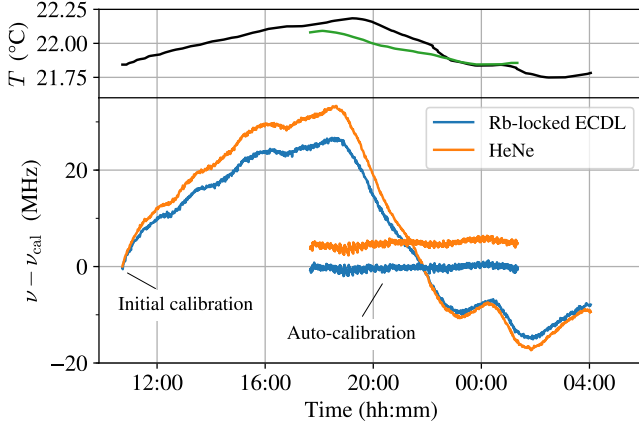


Figure 8: Long-term frequency drifts in the readout of the WSU-30 for the HeNe laser (orange) and the Rb-locked ECDL (blue). Lower panel: deviation of the frequency readout  $\nu$  to the frequency readout at the time of calibration  $\nu_{\text{cal}}$ . The measurement was performed two times: firstly with one initial calibration and secondly with auto-calibration (AC) in a 10 min interval to the Rb-locked ECDL. For better readability the HeNe frequency has an offset of +5 MHz in the measurement with AC. Upper panel: temperature readout of the WSU-30 for the measurement without AC (black) and with AC (green).

delay of around 6 ns between excitation and ionization laser pulses was implemented to find the optimal compromise between linewidth reduction and scan time [32]. The obtained FWHM of the resonances was between 110-130 MHz, including the natural linewidth, the Fourier-limited amplified TA:pro laser linewidth ( $\approx 70$  MHz) and some residual power broadening from the ionization laser. In addition, for the in-gas-jet data, a resolution of  $\approx 400$  MHz was achieved, consisting of the components already mentioned added to a  $T \approx 22$  K Doppler ensemble in a Mach 7.5 jet. The final results for the hyperfine parameters of  $^{63,65}\text{Cu}$  are summarized in Table II. These values are obtained after evaluation with the Statistical Analysis Toolbox for Laser Spectroscopy (SATLAS) module in python [33]. This software is designed specifically to analyze the data of laser spectroscopy experiments and allows for both  $\chi^2$  and maximum likelihood fitting procedures. A model for the hyperfine structure of the element of interest is fitted directly to the experimental spectrum, providing both hyperfine parameters and resonance characteristics. From Table II, a consistent and reproducible disagreement  $> 10\sigma$ , with literature on the value  $a(^{63}\text{Cu,g.s.})$  is found. The WS7-60 to SFPI comparison in Fig. 10 shows, however, an overestimation of the relative distances, defining for example the  $^{63}\text{Cu}$  ground-state splitting, as indicated by the relative difference in position on the  $\Delta_{\text{SFPI-WS7}}(\nu)$  function of the particular resonances in the figure. Therefore, to improve the WS7-60's precision, the wavelength array in

the hyperfine spectra is corrected by a fit of the waveform in Fig. 10. Because the fine structure of  $\Delta_{\text{SFPI-WS7}}(\nu)$  as a function of wavelength is much more complex than a triangular waveform, a spline generated by the *splrep* function of the *scipy* python library, weighted by the errors on each measurement point, was used to describe its behavior by finding the B-spline representation of the curve. The distribution of residuals from this spline were used to define  $\Delta\nu_{\text{corr}} \approx 1$  MHz. The resulting hyperfine parameters, obtained after correcting the wavelength array of each scan by the spline function, are shown in Table II. This correction procedure alters the readout of the WS7-60 such that it would match that of the SFPI reference. Agreement with literature is obtained for  $^{63,65}\text{Cu}$  within  $1\sigma = 0.5(^{63}\text{Cu}), 0.8(^{65}\text{Cu})$  MHz for the ABU, and  $1.25\sigma = 2$  MHz for the gas jet, respectively, taking into account only statistical errors. This correspondence means that with the correction applied to the WS7-60 output, an uncertainty  $\Delta\nu_{\alpha\beta,\text{total}}^{654,98} = 3$  MHz is achieved in this specific wavelength region. Combining the results for both hyperfine  $a$  parameters of  $^{63,65}\text{Cu}$ , reveals  $a(^{63}\text{Cu,g.s.})/a(^{63}\text{Cu,e.s.}) = 1.600(11)$  and  $a(^{65}\text{Cu,g.s.})/a(^{65}\text{Cu,e.s.}) = 11.620(17)$ , respectively, excluding any hyperfine anomaly within this precision. An isotope shift  $\delta\nu^{63-65}$  of 573.7(18) MHz can also be extracted from the data, also in agreement with literature [34, 35].

In case no spline correction were applied, an additional non-stochastic systematic error would have to be introduced to the resulting observables,  $a_{\text{Cu,g.s.}}$ ,  $a_{\text{Cu,e.s.}}$  and  $\delta\nu^{63-65}$ , such that  $\Delta\nu_{\alpha\beta,\text{total}}^{654,98}$  is bound by a specific condition from Table I. When no information is available on the wavelength meter response in the required range, the conservative absolute uncertainty of the device (60 MHz for WS7-60) should be taken into account.

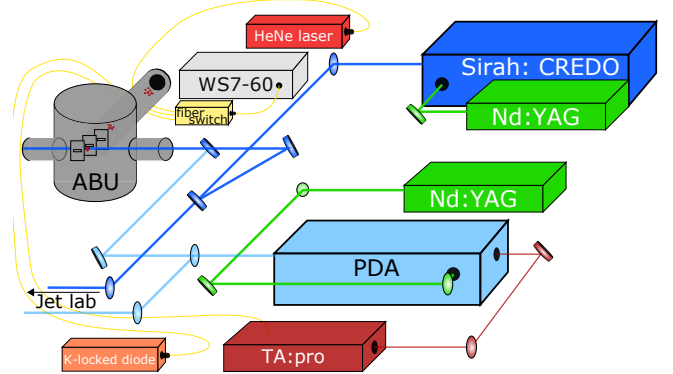


Figure 9: Schematic overview of the setup used to determine the hyperfine parameters of the  $4s\ ^2S_{1/2}$  to  $4p\ ^2P_{1/2}$  transition. For the in-gas-jet measurements, the UV laser beams were guided to the adjacent offline beam separator lab, see [15, 31].

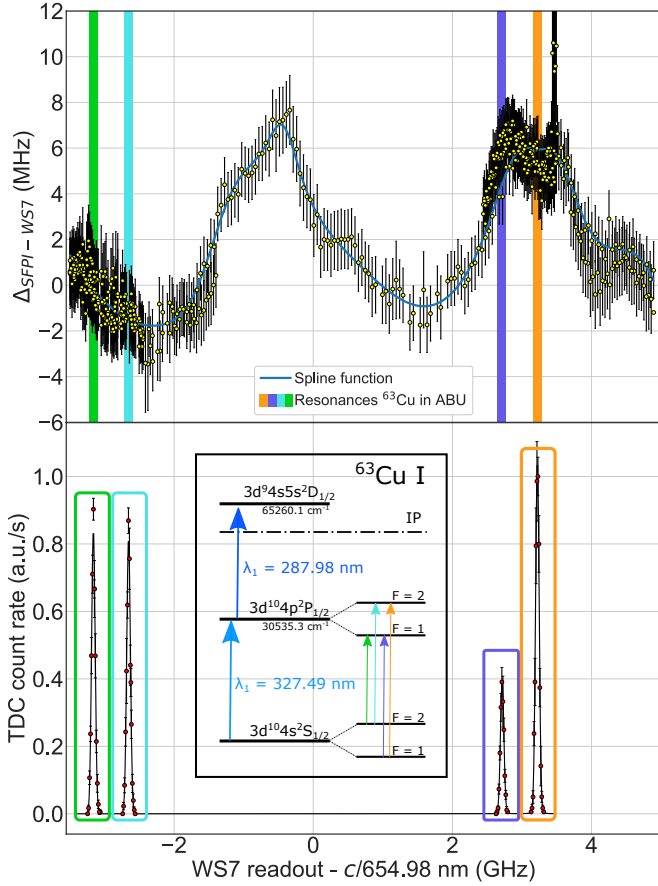


Figure 10: Visualization of the correction to the WS7-60 output. The upper panel shows a zoom of  $\Delta_{\text{SFPI-WSX}}(\nu)$  in the wavelength range of the  $4s^2S_{1/2}$  to  $4p^2P_{1/2}$  hyperfine structure in copper. The spline function corrects each individual wavelength number given by the WS7-60 during the frequency scan such that  $\Delta_{\text{SFPI-WSX}}(\nu) = 0$  and no apparent disagreement with the SFPI reference exists. The bottom panel shows a typical copper hyperfine spectrum with the fitted lineshape. All frequency values have been reported with respect to the fundamental wavelength, which is read by the wavelength meter. The results of the  $\Delta_{\text{SFPI-WSX}}(\nu) = 0$  correction on the hyperfine parameters are shown in table Table II.

## V. CONCLUSION

In this paper, two performance aspects of several commercial wavelength meters (HighFinesse GmbH), which are commonly used to monitor, stabilize and scan a laser's wavelength in medium/high-resolution laser hyperfine spectroscopy experiments, are investigated in a number of laboratories. First, the measurement uncertainty of wavelength differences in the order of 10 GHz,  $\Delta\lambda_{\alpha\beta}$ , which is directly related to the final physical observables of interest, is determined by a comparison to

Literature	$a(^{63}\text{Cu,g.s.})$ (MHz)	$a(^{63}\text{Cu,e.s.})$ (MHz)	
		5866.90871(2)	505.2 (8)
Experiment	$a(^{63}\text{Cu,g.s.})$ (MHz)	$a(^{63}\text{Cu,e.s.})$ (MHz)	
	ABU	5874.4(5)	505.0(5)
	ABU	5866.9(5)	505.8(5)
	Gas jet	5873(2)	506(2)
	Gas jet	5870(2)	506(2)

Literature	$a(^{65}\text{Cu,g.s.})$ (MHz)	$a(^{65}\text{Cu,e.s.})$ (MHz)	
		6284.38997(6)	542.9(16)
Experiment	$a(^{65}\text{Cu,g.s.})$ (MHz)	$a(^{65}\text{Cu,e.s.})$ (MHz)	
	ABU	6290.9(8)	539.9(8)
	ABU	6284.0(8)	541.0(8)

Table II: Literature values for the hyperfine parameters of the  $4s^2S_{1/2}$  to  $4p^2P_{1/2}$  transition in  $^{63}\text{Cu}$  and  $^{65}\text{Cu}$  compared to results obtained for the measurements in the ABU and in a gas jet. The correction to the WS7-60 wavelength meter output, discussed in the text, was applied to the data with the  $\bar{X}$  mark [34–37].

both an SFPI and a GPS-referenced frequency comb. For these frequency differences, induced by the hyperfine interaction, it was observed that the wavelength meters, which were all performing within specifications of the manufacturer, exhibit reproducible, quasi-periodic wavelength and device-dependent discrepancies with other reference sources, with the period lying close to the free spectral range of the device's most precise interferometer. This rather inexpensive, practical and simple characterization allows for a firm determination of the  $\Delta\lambda_{\alpha\beta}$  in the wavelength range of interest. Either  $\Delta\lambda_{\alpha\beta}$  can be reduced to the measurement uncertainty of the comparison, by correcting the observed periodic behavior or, the peak-to-peak discrepancy of the observed pattern is used to define an additional systematic uncertainty  $\Delta\lambda_{\alpha\beta}$ . In case no comparison is performed, the absolute uncertainty, quoted by the manufacturer, remains the only trustworthy source for  $\Delta\lambda_{\alpha\beta}$ . This procedure was validated by laser spectroscopy on  $^{63-65}\text{Cu}$  isotopes in an Atomic Beam Unit (ABU) and in a gas jet. Finally, to ensure stable performance when probing rare exotic isotopes over longer times, two different solutions are validated, both taking advantage of an external reference source's wavelength stability. In conclusion the quoted absolute measurement uncertainty of the specific wavelength meter should coincide with the expected attainable precision on the physical observables of the experimental laser-spectroscopy technique. In case the former significantly exceeds the latter, an extra characterization of the wavelength meter, as described here, should be performed in the specific wavelength range of interest in order to provide a trustworthy estimate of the measurement uncertainty. This statement, alongside complementary investigations discussed here and in [1], should provide guidelines for users of these devices, both in their



operation and in potential new acquisitions.

### ACKNOWLEDGMENTS

This work has received funding from Research Foundation Flanders (FWO, Belgium), from the Excellence of Science program (EOS, FWO-FNRS, Belgium), by GOA/2015/010 and STG/15/031 (BOF KU Leuven), by the Interuniversity Attraction Poles Program initiated by the Belgian Science Policy Office (BriX network P7/12), from the European Union's Horizon 2020 research and innovation program under Grants Agreement No. 654002 (ENSAR2), from the European Re-

search Council under the European Union's Seventh Framework Program (ERC-2011-AdG-291561-HELIOS), from the German Federal Ministry of Educations and Research (BMBF) under contracts 05P19RDFN1 and 05P18RFCIA and from the German Research Foundation (DFG) under contract DU 1134/1-2. M.V. is supported by an FWO grant (Aspirant - 1121820N). A significant share of the research work described herein originates from R&D carried out in the frame of the FAIR Phase-0 program of LASPEC/NUSTAR. The authors would like to thank both F. Karlewski (HighFinesse) for his efforts and the fruitful discussions and P. Imgram (TU Darmstadt) for his support with the transfer cavity setup at JYFL.

- 
- [1] K. König, P. Imgram, J. Krämer, B. Maaß, K. Mohr, T. Ratajczyk, F. Sommer, and W. Nörtershäuser, 'On the performance of wavelength meters -- Part 2: Frequency-comb based characterization revealing their relative limitations and offering opportunities for more accurate absolute wavelength determinations', submitted for publication in *Applied Physics B* (2019).
- [2] B. Sanguinetti, H. O. Majeed, M. L. Jones, and B. T. Varcoe, *J. Phys. B: At. Mol. Opt. Phys.* **42**, 165004 (2009).
- [3] K. Saleh, J. Millo, A. Didier, Y. Kersalé, and C. Lacroûte, *Appl. Opt.* **54**, 9446 (2015).
- [4] L. Couturier, I. Nosske, F. Hu, C. Tan, C. Qiao, Y. H. Jiang, P. Chen, and M. Weidemüller, *Rev. of Sci. Instrum.* **89**, 043103 (2018).
- [5] L. A. Johnson, H. O. Majeed, B. Sanguinetti, T. Becker, and B. T. Varcoe, *New J. Phys.* **12**, 063028 (2010).
- [6] A. Koszorus, 'Precision measurements of the charge radii of potassium isotopes', accepted for publication *Phys. Rev. C* (2019).
- [7] K. Blaum, J. Dilling, and W. Nörtershäuser, *Phys. Scrip.* **T152** (2013).
- [8] P. Campbell, I. D. Moore, and M. Pearson, *Prog. Part. Nucl. Phys.* **86** (2016).
- [9] V. N. Fedosseev, Y. Kudryavtsev, and V. I. Mishin, *Phys. Scr.* **85**, 058104 (2012).
- [10] B. A. Marsh, T. Day Goodacre, S. Sels, Y. Tsunoda, B. Andel, A. N. Andreyev, N. A. Althubiti, D. Atanasov, A. E. Barzakh, J. Billowes, K. Blaum, T. E. Cocolios, J. G. Cubiss, J. Dobaczewski, G. J. Farooq-Smith, D. V. Fedorov, V. N. Fedosseev, K. T. Flanagan, L. P. Gaffney, L. Ghys, M. Huyse, S. Kreim, D. Lunney, K. M. Lynch, V. Manea, Y. Martinez Palenzuela, P. L. Molkanov, T. Otsuka, A. Pastore, M. Rosenbusch, R. E. Rossel, S. Rothe, L. Schweikhard, M. D. Seliverstov, P. Spagnoletti, C. Van Beveren, P. Van Duppen, M. Veinhard, E. Verstraelen, A. Welker, K. Wendt, F. Wienholtz, R. N. Wolf, A. Zadornaya, and K. Zuber, *Nature Physics* **14**, 1163 (2018).
- [11] R. Ferrer, A. Barzakh, B. Bastin, R. Beerwerth, M. Block, P. Creemers, H. Grawe, R. de Groote, P. Delahaye, X. Fléchar, S. Franchoo, S. Fritzsche, L. P. Gaffney, L. Ghys, W. Gins, C. Granados, R. Heinke, L. Hijazi, M. Huyse, T. Kron, Y. Kudryavtsev, M. Laatiaoui, N. Lecesne, M. Loiselet, F. Lutton, I. D. Moore, Y. Martínez, E. Mogilevskiy, P. Naubereit, J. Piot, S. Raeder, S. Rothe, H. Savajols, S. Sels, V. Sonnenschein, J. C. Thomas, E. Traykov, C. Van Beveren, P. Van den Bergh, P. Van Duppen, K. Wendt, and A. Zadornaya, *Nature Communications* **8**, 14520 (2017).
- [12] S. Raeder, T. Kron, R. Heinke, J. L. Henares, N. Lecesne, P. Schönberg, M. Trümper, and K. Wendt, *Hyperfine Interact.* **238**, 15 (2017).
- [13] R. Neugart, J. Billowes, M. Bissell, K. Blaum, B. Cheal, K. Flanagan, G. Neyens, W. Nörtershäuser, and D. T. Yordanov, *J. Phys. G* **44** (2017).
- [14] Y. Kudryavtsev, R. Ferrer, M. Huyse, P. Van den Bergh, and P. Van Duppen, *Nucl. Instrum. Methods B* **297**, 7 (2012).
- [15] K. Dockx, T. E. Cocolios, R. Ferrer, C. Granados, S. Kraemer, Y. Kudryavtsev, S. Sels, P. Van den Bergh, P. Van Duppen, M. Verlinde, E. Verstraelen, and A. Zadornaya, *Nucl. Instrum. Methods B* **463**, 297 (2020).
- [16] S. Rothe, B. A. Marsh, C. Mattolat, V. N. Fedosseev, and K. Wendt, *J. Phys.: Conference Series* **312**, 052020 (2011).
- [17] S. Raeder, S. Fies, H. Tomita, K. D. A. Wendt, T. Iguchi, and K. Watanabe, in *AIP Conference Proceedings* (AIP, 6–10 October 2008) pp. 96–101.
- [18] H. Tomita, C. Mattolat, T. Kessler, S. Raeder, F. Schweltnus, K. D. A. Wendt, K. Watanabe, and T. Iguichi, *J. Nucl. Sci. Technol.* **45**, 37 (2008).
- [19] V. Sonnenschein, S. Raeder, A. Hakimi, I. D. Moore, and K. Wendt, *J. Phys. B* **45**, 165005 (2012).
- [20] A. Hakimi, T. Fischbach, S. Raeder, N. Trautmann, and K. Wendt, *Hyperfine Interact.* **216**, 59 (2013).
- [21] R. Heinke, T. Kron, S. Raeder, T. Reich, P. Schönberg, M. Trümper, C. Weichhold, and K. Wendt, *Hyperfine Interact.* **238**, 127 (2017).
- [22] T. Kessler, H. Tomita, C. Mattolat, S. Raeder, and K. Wendt, *Laser Phys.* **18**, 842 (2008).
- [23] V. Sonnenschein, I. D. Moore, S. Raeder, M. Reponen, H. Tomita, and K. Wendt, *Laser Phys.* **27**, 085701 (2017).
- [24] W. Zhao, J. Simsarian, L. Orozco, and G. Sprouse, *Rev. Sci. Instrum.* **69**, 3737 (1998).
- [25] D. Studer, J. Ulrich, S. Braccini, T. S. Carzaniga, R. Dressler, K. Eberhardt, R. Heinke, U. Köster,

- S. Raeder, and K. Wendt, *Eur. Phys. J. A* **56**, 69 (2020).
- [26] J. Krämer, K. König, C. Geppert, P. Imgram, B. Maaß, J. Meisner, E. Otten, S. Passon, T. Ratajczyk, J. Ullmann, and W. Nörtershäuser, *Metrologia* **55**, 268 (2018).
- [27] P. Imgram, K. König, J. Krämer, T. Ratajczyk, R. Müller, A. Surzhykov, and W. Nörtershäuser, *Phys. Rev. A* **99**, 012511 (2019).
- [28] I. Moore, T. Eronen, D. Gorelov, J. Hakala, A. Jokinen, A. Kankainen, V. Kolhinen, J. Koponen, H. Penttilä, I. Pohjalainen, M. Reponen, J. Rissanen, A. Saastamoinen, S. Rinta-Antila, V. Sonnenschein, and J. Äystö, *Nucl. Instrum. Methods B* **317**, 208 (2013), xVIth International Conference on ElectroMagnetic Isotope Separators and Techniques Related to their Applications, December 2–7, 2012 at Matsue, Japan.
- [29] R. de Groote, A. de Roubin, P. Campbell, B. Cheal, C. Devlin, T. Eronen, S. Geldhof, I. Moore, M. Reponen, S. Rinta-Antila, and M. Schuh, *Nucl. Instrum. Methods B* **463**, 437 (2019).
- [30] B. Cheal, M. Gardner, M. Avgoulea, J. Billowes, M. Bissell, P. Campbell, T. Eronen, K. Flanagan, D. Forest, J. Huikari, A. Jokinen, B. Marsh, I. Moore, A. Nieminen, H. Penttilä, S. Rinta-Antila, B. Tordoff, G. Tungate, and J. Äystö, *Phys. Lett. B* **645**, 133 (2007).
- [31] A. Zadornaya, P. Creemers, K. Dockx, R. Ferrer, L. P. Gaffney, W. Gins, C. Granados, M. Huysse, Y. Kudryavtsev, M. Laatiaoui, E. Mogilevskiy, S. Raeder, S. Sels, P. Van Den Bergh, P. Van Duppen, M. Verlinde, E. Verstraelen, M. Nabuurs, D. Reynaerts, and P. Papadakis, *Phys. Rev. X* **8**, 41008 (2018).
- [32] R. P. De Groote, M. Verlinde, V. Sonnenschein, K. T. Flanagan, I. Moore, and G. Neyens, *Phys. Rev. A* **95**, 1 (2017).
- [33] W. Gins, R. P. de Groote, M. L. Bissell, C. Granados Buitrago, R. Ferrer, K. M. Lynch, G. Neyens, and S. Sels, *Comput. Phys. Commun.* **222**, 286 (2018).
- [34] P. Vingerhoets, *Nuclear structure of Cu isotopes studied with collinear laser spectroscopy*, Ph.D. thesis, KU Leuven (2011).
- [35] G. Hermann, G. Lasnitschka, C. Schwabe, and D. Spengler, *Spectrochim. Acta, Part B* **48B**, 1259 (1993).
- [36] H. Figger, D. Schmitt, and S. Penselin, *Colloq. Int. C.N.R.S* **164** (1967).
- [37] H. Bucka, J. Ney, and P. Wirtnik, *Zeitschrift für Physik* **202**, 22 (1967).